Received 14 September 2022; revised 18 October 2022; accepted 21 October 2022. Date of publication 2 November 2022; date of current version 18 November 2022.

Digital Object Identifier 10.1109/OJAP.2022.3218798

High-Temperature Additively Manufactured C-Band Antennas Using Material Jetting of Zirconia and Micro-Dispending of Platinum Paste

CARLOS R. MEJIAS-MORILLO[1], JAYAPRAKASH B. SHIVAKUMAR[1], SENG LOONG YU[1], BLAKE ROBERTS[1], PEDRO CORTES[2], ERIC MACDONALD[3] (Senior Member, IEEE), ANTON V. POLOTAI[4], AND EDUARDO A. ROJAS-NASTRUCCI[1]

[1]Department of Electrical Engineering and Computer Science, Embry-Riddle Aeronautical University, Daytona Beach, FL 32114, USA

[2]Department of Civil/Environmental and Chemical Engineering, Youngstown State University, Youngstown, OH 44555, USA

[3]Department of Aerospace and Mechanical Engineering, The University of Texas at El Paso, El Paso, TX 79968, USA

[4]Department of Dielectric Research and Development, Vibrantz Technologies, Penn Yan, NY 14527, USA

CORRESPONDING AUTHOR: E. A. R.-NASTRUCCI (e-mail: rojase1@erau.edu)

This work was supported in part by the National Science Foundation under Grant 1944599, and in part by the ADMETE Grant from the AFRL under Grant FA8650-20-2-1136.

ABSTRACT Additive manufacturing (AM) enables the development of rapid, low-cost prototypes for ad-hoc and on-demand manufacturing to repair and keep up the continuous operation of systems, especially in time-sensitive scenarios where the system recovery cannot wait for the shipment of new components. Therefore, the industry, military, and academia continue to invest in these technologies to potentially achieve novel 3D geometries based on high-temperature dielectric and conductors to endure harsh environments, such as commonly found in the oil and gas, defense, and aerospace sectors. This paper reports the electromagnetic properties of 3D-printed Yttria-Stabilized Zirconia (YSZ) for 2-6 GHz and the DC and RF effective conductivity of sintered platinum ink, where the dissipative losses of the additively manufactured coplanar waveguides (CPWs) are less than 0.05 dB/mm when the frequency is below 4 GHz. In addition, the AM CPWs are exposed to thermal cycling up to 600 °C to study the material's thermal fatigue and potential degradation. However, the samples do not exhibit appreciable degradation after thermal cycling. Also, a two-layer back-fed antenna based on 3D-printed YSZ and platinum ink is designed, manufactured, and tested. Results show a measured gain of 2.5 dBi and a front-back ratio of 9.6 dB at 4.1 GHz.

INDEX TERMS Additive manufacturing, antenna, ceramic substrate, coplanar waveguide, high-temperature antenna, material jetting, microdispensing, platinum, stencil printing, thermal fatigue, zirconia.

I. INTRODUCTION

WIRELESS sensing in harsh environments has become a prominent field of study during the last two decades, especially in the oil and gas, defense, and aerospace sectors. High temperature is one of the prevailing physical conditions in aircraft and spacecraft's operating environment, where it can reach temperatures up to 2760 °C when they approach hypersonic speeds [1], [2]. Therefore, it is essential to use high-temperature dielectric and conductive materials to survive such extreme conditions and avoid overheating the components of the communication systems in the space launch vehicles or aircraft. Furthermore, as the Mach number increases under hypersonic conditions, the antenna systems are prone to high-temperature ablation and large temperature gradients, leading to changes in the material's electrical properties that affect the antenna parameters such as impedance bandwidth, radiation pattern, antenna gain, antenna beamwidth, among others.

This work is licensed under a Creative Commons Attribution 4.0 License. For more information, see https://creativecommons.org/licenses/by/4.0/

Wireless sensors have found their way into the aerospace industry since the emergence of the wireless sensing topic in the mid of the 1990s. The wireless sensing technology provides many benefits, such as low power consumption, low-cost maintenance, low weight, easy installment, and high reliability [3], [4]. The multiple advantages of wireless sensors have exponentially increased the interest and demand for passive wireless sensors in high-temperature environments such as gas paths and blades of gas-turbine engines to monitor their real-time health since combustion turbines are the primary propulsion system for commercial and military aircraft [4], [5]. Therefore, the wireless communication system, i.e., the interrogator antenna and the sensors, must withstand the aircraft engine's extreme conditions, where the corrosive-gas environment can reach a temperature up to 1600 °C.

Similarly, space exploration for the inner part of the Solar system, i.e., Venus, Mercury, and the Sun, requires RF/microwave devices to operate for thousands of hours at high temperatures. The National Aeronautics and Space Administration (NASA) is currently working on a small probe, called Long-Lived In-Situ Solar System Explorer (LLISSE), to receive and transmit low data volume measurements from the Venus surface for at least 60 Earth days [6]. In addition, the European Space Agency (ESA), in cooperation with the Japan Aerospace Exploration Agency (JAXA), sent a space probe to Mercury in 2018, which comprised of two orbiters: Mercury Planetary Orbiter (MPO) and Mercury Magnetospheric Orbiter (Mio). These two spacecraft will be orbiting the planet at the same time by 2025 [7]. Beyond that, the scientific community demands continuity of space exploration of Mercury, by using landed probes to understand Mercury's thermochemical evolution better. However, landed probes must be capable of enduring high temperatures up to 400 °C.

Ceramic materials have been extensively adopted in the aerospace industry since the late 50's for high-temperature applications. Ceramics have unique characteristics such as a high melting point and good mechanical properties, besides being chemically inert [8], [9]. However, ceramic processing requires specialized tools and many hours of labor to meet the design specifications, making it expensive and complicated, particularly for prototyping. Furthermore, conventional ceramic processes typically constrain the geometry of the object.

Since additive manufacturing (AM) can enable low-cost rapid prototyping, ad-hoc fabrication, and repair of passive microwave components to maintain the continuous operation of wireless communication systems, the research community continues investigating AM techniques to create 3D-printed microwave devices using ceramic thermoplastic composites, as well as ceramic-resin composites for enduring high temperatures [10], [11], [12], [13]. E.g., It has been demonstrated that a 3D-printed Zirconia helical antenna with a reduced radar cross-section has a similar performance to conventional metal antennas [13]. Furthermore, [12], it has been shown that 3D-printed Zirconia dielectric resonator antennas (DRA) exhibit a dielectric constant of 23 and a loss tangent of 0.0013. Also, laser-based digital manufacturing techniques have been used to achieve high-temperature wireless sensors [14]. Electromagnetic properties that make them suitable for designing smaller and superior high-efficiency antennas. However, no previous works have characterized the antenna performance after a high-temperature exposure.

Regarding high-temperature environments, the material properties of the antenna are temperature dependent due to the chemical reactions caused by the heat increments. Therefore, the design of high-temperature antennas must consider that the metal layers have low chemical reactivity to avoid oxidation and corrosion caused by the heat of the harsh environment [15], [16]. Noble metals, such as platinum (Pt), silver (Ag), palladium (Pd), gold (Au), Rhodium (Rd), and Iridium (Ir), are highly resistant to corrosion, as well as the alloys made of them [17]. Platinum is the most widely used noble metal in harsh environment applications due to its high melting point (1768 °C) and low chemical reactivity at high temperatures. Studies have reported the use of platinum for passive wireless sensors and antennas, as shown in [18], [19], [20], [21], [22], [23], [24], [25], [26], [27], [28]. However, the thermal behavior and the RF characteristic of a micro-dispensed platinum ink have not been documented at this time.

This work compares the electromagnetic properties of an antenna based on a commercial Yttria-Stabilized Zirconia (YSZ), and a material jetted 3D-printed YSZ, where the relative permittivity is extracted from the S-parameters of a coplanar waveguide (CPW) placed on the top of the ceramic substrates. In this paper, both materials are measured, and the results show similar values of high permittivity and losses up to 6 GHz. Furthermore, the DC conductivity and effective RF conductivity of the sintered platinum ink are characterized at room temperature and after nine cycles at high temperature (600 °C). Note that the CPW samples made of ceramic substrates and the platinum ink exposed to high-temperature cycles do not exhibit appreciable thermal fatigue or significant degradation of the RF performance. Additionally, a fully 3D-printed CPW back-fed antenna using Direct-Ink-Writing (DIW) is designed, manufactured, and tested. The additively manufactured antenna is based on combining material jetting and ink micro-dispensing to create the ceramic substrate and the metal layers, respectively. As a result, the 3D-printed antenna shows a gain of 2.5 dBi and 3.9% of the bandwidth for return loss $\geq$ 10 dB at 4.1 GHz. Fig. 1 shows an illustration of an additively manufactured back-fed antenna based on material jetting and microdispensing in a high-temperature environment.

II. ADDITIVE MANUFACTURING PROCESS

This paper presents a fully additively manufactured antenna by combining two manufacturing processes, i.e., material jetting and microdispensing. The first method creates a

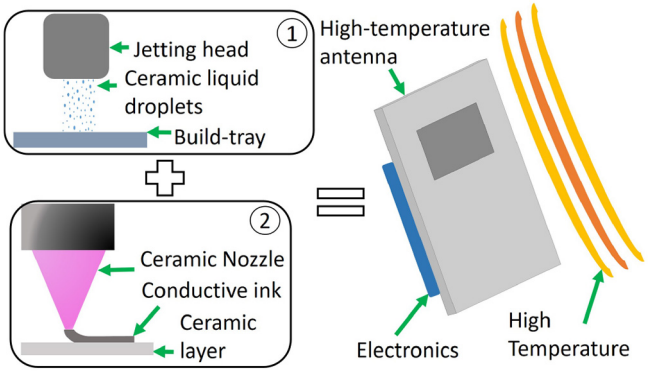

FIGURE 1. Additively manufactured antenna in a harsh environment.

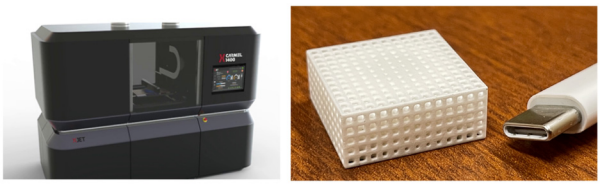

FIGURE 2. XJET Carmel 1400C (xjet.com) and an example spatially-varying zirconia lattice with 1 mm unit cells.

3D-printed ceramic substrate, and the second produces a metal film of the antenna pattern on both sides of the ceramic substrate with conductive ink that endures high temperatures. A second traditional manufacturing method, stencil printing, is used to manufacture a second antenna for benchmark of the fully additively manufactured version.

A. MATERIAL JETTING PROCESS

Material jetting is one of the seven additive manufacturing categories as defined by the ASTM F42 Standard [29]. The ink-jet-based process employs the ejection of a fluid, typically with viscosity limited to between 20-40 cP [30], [31], and employs hundreds of ink jet ports allowing for rapid multi-material parallel deposition. Recent developments in solution-based ink jetting in which nanoparticles are delivered in the liquid (serving as a carrier solution) have produced ceramic parts with high-resolution features. The XJet Carmel 1400C 3D printer used in this study, shown below in Figure 2 (left), relies on NanoParticle Jetting^{TM}(NPJ), which is a type of solution-based material jetting. This approach involves the dispersion of nanoparticles of either metal or ceramic suspended in a liquid solution. With the resolution of ink jetting (20 μm after sintering and shrinkage), intricately-detailed geometries have been fabricated with a layer thickness of about 10 μm [32]. A thermal post-processing sintering stage (typically 1450 °C for 40-60 hours) is required for the nano-sized particles to reach nearly-full density as a structure [32]. Fig. 2 (right) illustrates a spatially-varying lattice with 1 mm unit cell size and strut and beam features with widths as low as 250 μm.

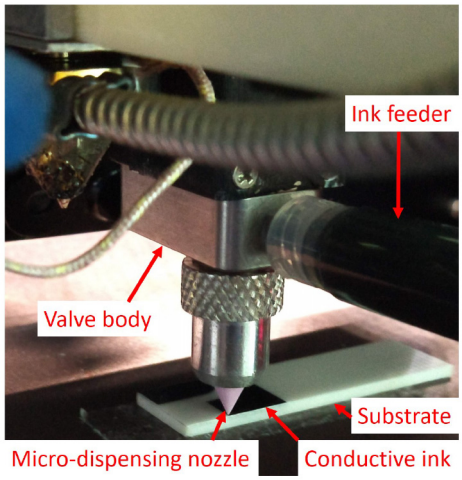

FIGURE 3. Microdispensing of platinum ink on ceramic substrate.

B. MICRODISPENSING PROCESS

The metal patterning on the ceramic substrate is created by a SmartPump placed into a nScrypt 3Dn-Tabletop. The SmartPump is a positive-pressure pump where liquids or pastes, pressurized with air on a dispensing barrel, are micro-dispensed using a vertical valve close to the dispensing nozzle to control the material flow. The SmartPump achieves dispensed volume control out of the nozzle in the order of a hundred picoliters. The ink is pushed through a ceramic nozzle with an inner diameter of 125 μm, and an outer diameter of 175 μm. The positive pressure in the pump is set at 7 psi while the dispensing nozzle moves at 15 mm/s at 80 μm above the surface to ensure a uniform ink distribution along the surface. Fig. 3 shows the result of microdispensing platinum ink on a ceramic substrate using the SmartPump of a nScrypt system. Once the ink patterning of the layer is done, the ink rests for 10 min. Then, the ink is dried at a low temperature between 120 - 125 °C for 30-60 min under air atmosphere conditions to evaporate the organic agents of the conductive ink and increase the mechanical strength and the electrical conductivity of the metal traces.

III. MATERIAL CHARACTERIZATION

A. HIGH-K ADDITIVELY MANUFACTURED CERAMIC SUBSTRATE

This paper compares the electrical properties between the commercial YSZ and the 3D-printed YSZ. The electrical permittivity of the material is extracted from the propagation constant ($\gamma = \alpha + j\beta$) based on the S-parameters of a CPW transmission line as described in [33]. Note that the CPW method enable a wideband characterization of permittivity by using a single 3D-printed sample, which are usually doable considering the size restriction of 3D printers. The material permittivity is calculated as

$$\varepsilon_r = \frac{\varepsilon_{eff} - 1}{q} + 1 \tag{1}$$

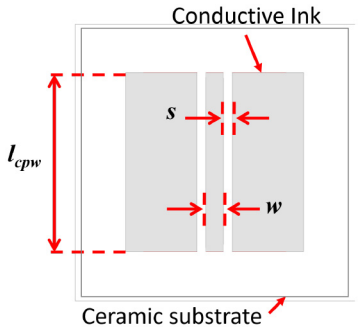

FIGURE 4. Geometric parameters of the CPW.

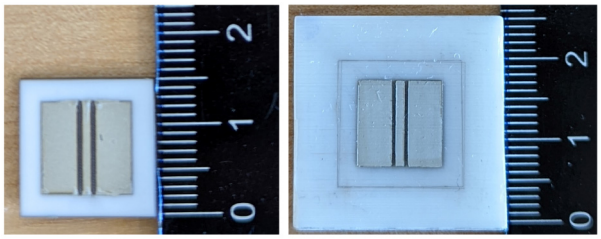

(a) CPW on commercial YSZ (b) CPW on 3D-printed YSZ

FIGURE 5. Laser-processed stencil-printed silver CPW on commercial YSZ and 3D-printed YSZ substrates (scale in cm).

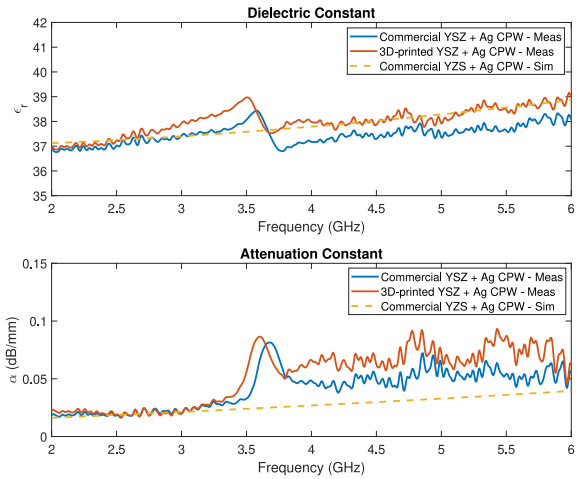

FIGURE 6. Dielectric properties of commercial YSZ and 3D-printed YSZ using silver stencil-printed CPWs.

where q is the dielectric filling factor that depends on the CPW geometry. The effective dielectric constant ε_{eff} is defined as $\frac{\beta^2-\alpha^2}{\omega^2\mu}$, considering that ω is the angular frequency.

An LPKF U4 laser machine processes the 0.94 mm thick commercial substrate, which is doped with 3.5% mol density of yttria, to get square YSZ samples of 15 mm x 15 mm, while an XJET 1400C Carmel system creates a 24.6 x 24.8 x 1.57 mm^3 YSZ sample.

To pattern the conductive traces and ground plane of the CPW, a 60 μm thick PET tape is laser-cut by the LPKF Protolaser U4 to create a stencil of the CPW, which is placed on the substrate, as shown in [34]. The LPKF Protolaser U4 uses a 355 nm wavelength UV laser with a ~20 μm diameter focus, which enables the micro-machining of the PET tape to create the PET stencil without damaging the substrate below. First, the PET tape is cut by the LPKF Protolaser U4's default properties of the top isolation task from the structure toolpath. Once the cut is done, the PET tape is removed in the areas that will be filled with conductive ink. Then, the conductive ink is distributed uniformly over the PET stencil by a metal squeegee blade with a bevel angle of 20 °C. Since this stencil printing is a manual process, there is no control of the squeegee angle and print speed. Finally, the conductive ink is dried in the same condition as the microdispensed ink.

The dimensions of the CPW line to create the PET stencil are shown in Fig. 4, where the central strip (w) is 1 mm width, and the slot (s) is 0.5 mm width. The CPW lines are made of Dupont CB028 silver paste to benchmark the electromagnetic properties of the ceramic substrates before exposing them to high temperatures since it dries at a low temperature of 120 °C for 30 min without requiring sintering later. The CB028 silver past has been extensively characterized [11], [35], [36], making an optimal ink to explore the properties of new dielectric materials. After the ink is cured, the PET stencil is removed, and an LPKF U4 laser machine processes the CPW line to remove the remaining ink in the slots of the CPW.

Fig. 5 shows the result of laser processing the stencil-printed CPW using silver ink for both samples, the 3D-printed YSZ substrate and the commercial YSZ substrate. The stencil transfer efficiency is verified by the aperture area ratio, which is calculated based on the CPW dimensions and the PET tape thickness. The three apertures of the CPW line have a ratio greater than 0.66, which guarantees that most of the ink is transferred to the ceramic substrate. A Filmetrics 3D optical profilometer, model Profilm3D, measures the surface profile of the dried silver ink, which shows a mean thickness of 12 μm. By comparing this result with the microdispensed shown in [37], the thicknesses of the dried silver ink are similar, confirming that the ink transfer by the PET stencil is satisfactory.

B. ELECTROMAGNETIC CHARACTERIZATION OF COMMERCIAL AND 3D-PRINTED YSZ

A Keysight N5227B PNA and two GGB Picoprobe 40A-GSG-1250-DP probes are calibrated from 2 GHz to 6 GHz using SOLT standards on a GGB CS-10 calibration substrate to measure the S-parameters of the stencil-printed silver CPW samples. Fig. 6 exhibits the electrical properties of the commercial YSZ sample and the 3D-printed YSZ sample extracted by measuring the S-parameters of the silver CPW samples. The relative dielectric constant of the 3D-printed YSZ at 5 GHz is 36.5, while the commercial YSZ at 5 GHz is 35.5. Fig. 6 also suggests that the contribution of the dielectric losses in the attenuation constants is slightly higher for the 3D-printed YSZ since both silver CPW samples are created with the same ink and the

same manufacturing process. The additional losses in the dielectric can be attributed to the remaining impurities and porousness presented after sintering the ceramic substrate. Both samples show a peak in the attenuation constant around 3.6 GHz, which is an effect of the half-wave resonance of the transmission line, as described in [38].

Attenuation constant measurements show that the CPW dimensions allow propagation of high-order modes after $\sim$ 7 GHz, which is consistent with the theoretical estimation in [39] eq. (2).

$$f_{\max} \cong \frac{1}{\mathrm{Max}\left\{h, \frac{w}{2}+s+g\right\}\sqrt{2\mu_0\epsilon_0(\epsilon_r-1)}} \tag{2}$$

C. ESL-5542 INK - PLATINUM INK

Since platinum (Pt) is a noble metal that withstands corrosive environments and high temperatures, this paper studies the electrical properties of an unfritted platinum ink called Ferro 5542 (ESL legacy), which is used to metalize the traces of the CPWs and the high-temperature antennas on the commercial and 3D-printed YSZ substrates.

1) PROPERTIES

Ferro 5542 is a commercially available fritless platinum metallization compatible with ceramic substrates. In earth-bound applications, it is stable to 900 °C. It is primarily used in gas sensors and solid oxide fuel cell applications. These properties make it worth evaluating in space applications operating at sustained high temperatures. This ink or paste is formulated for the screen printing deposition technique, not for stencil printing. However, as demonstrated in this study, this platinum ink can also be deposited using additive manufacturing techniques. The Ferro 5542 platinum ink can be fired in the range of 950 °C to 1.300 °C.

2) DC ELECTRIC CONDUCTIVITY MEASUREMENT

A 100 mm^2 square patch is stencil-printed on a 0.9 mm thick YSZ commercial substrate using platinum ink, which rests for 10 min at room temperature to level the ink before drying it. Then, the ink is dried at 125 °C for 1 hour. Later, the platinum square patch is sintered, i.e., raising the temperature at a rate of 30 °C/min until it reaches 980 °C, which is held at the peak temperature for 10 min, and then, the sample is cooled down to ambient temperature.

A Filmetrics 3D optical profilometer, model Profilm3D, extracted the surface profile of the platinum square patch before and after sintering, and it shows that the thickness of the platinum traces shrinks from 5 μm to $\sim$ 3.5 μm, equating to an approximate 30% shrinking during sintering.

The 10 x 10 mm^2 square patch is used to calculate the electrical conductivity of the sintered platinum ink by the four-point probe method shown in [40], where the electrical current is set at 0.3 A to get a detectable voltage. Considering that the thickness of the sintered platinum layer is $\sim$3.5 μm, the calculated electrical conductivity is $\sim$4 MS/m.

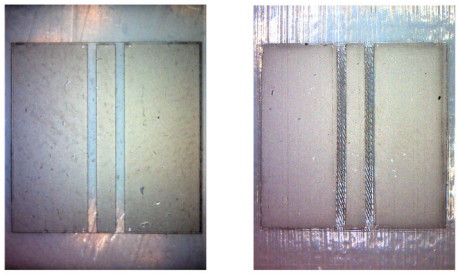

(a) Commercial (b) 3D-printed

FIGURE 7. Stencil-printed platinum CPW on commercial and 3D-printed YSZ substrates after sintering.

TABLE 1. Dimensions of the manufactured platinum CPW commercial YSZ substrate (units in mm).

Sample	w	s	l_{cpw}
Pt CPW on commercial YSZ	0.99	0.48	10.01
Pt CPW on 3D-printed YSZ	0.99	0.44	10.10

D. FULLY ADDITIVELY MANUFACTURED COPLANAR WAVEGUIDE

A stencil-printed platinum CPW on a 1.6 mm thick 3D-printed YSZ substrate is compared to another platinum CPW over a 0.9 mm thick commercial YSZ substrate. In both cases, the stencil-printed CPW has a gap of 0.5 mm, the central conductor is 1 mm, and the length of the transmission line is 10 mm. Both samples are visually inspected and electrically tested to ensure that the CPW traces are electrically isolated. The platinum ink of both CPWs is sintered to increase the platinum layer's electrical conductivity and mechanical properties. Fig. 7 exhibits the sintered platinum CPWs based on the stencil-printing process on the commercial and 3D-printed YSZ substrate. Table 1 shows the measured dimensions of the stencil-printed platinum ink on the commercial and 3D-printed YSZ substrate after sintering.

Fig. 8 shows the material permittivity for the commercial and 3D-printed YSZ substrates extracted from the platinum CPW transmission lines to verify that the sintering process of the ink does not affect the dielectric properties of the YSZ substrates. Results in Fig. 6 and Fig. 8 show close agreement between CPWs made of silver and platinum ink, exhibiting a difference of less than 1% between the extracted permittivity from the platinum CPW and the silver CPW. The minimal variations can be associated with the change in the conductive ink and curing or sintering cycles that affects the conductor thickness, as well as the variation in the RF probing process.

IV. HIGH-TEMPERATURE ANTENNA DESIGN

In this section, a high-temperature two-layer back-fed antenna is designed using the extracted electromagnetic properties of the YSZ substrates and the platinum conductive ink. Fig. 9 shows the geometric parameters of the high-temperature two-layer back-fed antenna, where the CPW line is tapered below the top patch to increase the coupling between the slot and the top patch, and it allows to tune

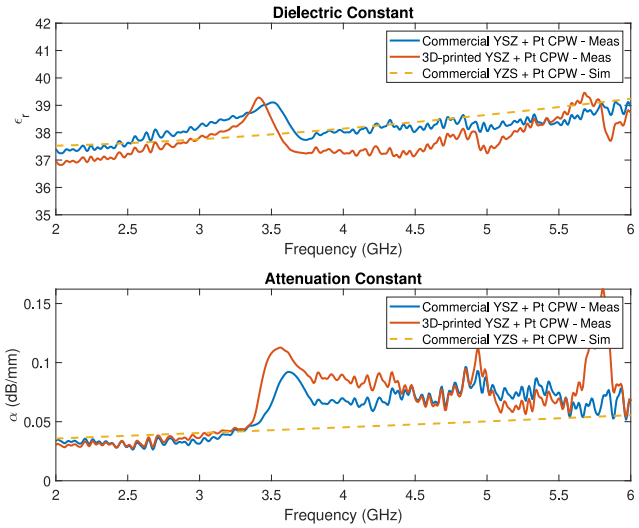

FIGURE 8. Dielectric properties of commercial YSZ and 3D-printed YSZ using platinum stencil-printed CPWs.

up the input impedance of the antenna to 50 Ω. Since the antenna is fed on the back of the substrate, the top patch can be placed outside of a package, which can protect the RF circuitry and the CPW line against harsh environmental conditions, such as high temperature. The antenna geometry is designed to yield a better front-back ratio than the slot antenna. Also, it simplifies the manufacturing process compared to the traditional coupled line microstrip antenna, which requires a multi-layer substrate.

The initial dimensions of the top patch are found by the design equations of the microstrip patch antenna considering the electrical permittivity of the 3D-printed and the commercial YSZ at 5 GHz and 4 GHz, respectively. Here, the CPW line and the tapered stub section are designed to provide 50 Ω at the antenna input at the resonant frequency. Then, the geometric parameters of the high-temperature two-layer back-fed antenna are optimized using HFSS from ANSYS Electronic Desktop 2019.0.0 for each material. Since the 3D-printed substrate has a dimension of 49.8 mm x 15.21 mm x 1.9 mm, the 3D-printed antenna is designed to fit the substrate size to be manufactured. Note that the RF connector is included in EM simulation of the antennas presented in this paper.

A. MANUFACTURING THE REFERENCE ANTENNA

Table 2 shows optimized parameters of the antenna based on the commercial YSZ substrate. This two-layer antenna is stencil printed on the commercial YSZ substrate using platinum ink, and then the ink is cured and sintered, as previously mentioned. Fig. 10 shows the sintered platinum antenna pattern on the commercial YSZ with a Cinch Connectivity Solutions end launch jack model 145-0701-802, which has a maximum operating temperature of 85 °C, so it cannot endure high temperatures. Therefore, it is required to remove the RF connector from the sample for high-temperature tests and re-install it after the high-temperature test is performed.

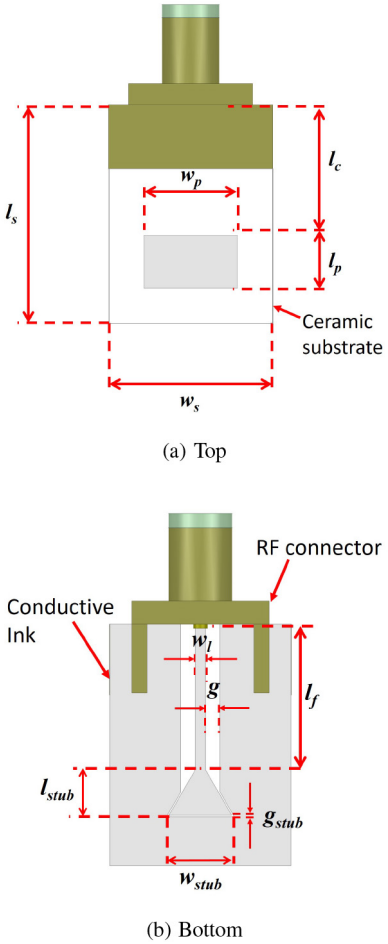

FIGURE 9. Structure of the two-layer coupled-fed microstrip antenna.

TABLE 2. Dimensions of the designed antenna based on commercial YSZ (units in mm).

w_p	l_p	l_c	l_s	w_s
7.17	4.06	10.40	16.76	12.57
w_l	g	l_f	l_{stub}	w_{stub}
0.7	1	10.1	3.14	4.33
g_{stub}				
0.1				

B. FULLY ADDITIVELY MANUFACTURED ANTENNA

The fully additively manufactured antenna is made of a 3D-printed YSZ substrate using an XJET Carmel 1400C and a micro-dispensed platinum ink by a SmartPump of a nScrypt system. Table 3 exhibits the geometric parameters of the optimized 3D-printed antenna. The manufacturing process of the two-layer antenna is based on micro-dispensing platinum ink over a 49.8 mm x 15.21 mm x 1.9 mm 3D-printed YSZ substrate. Initially, the bottom layer pattern is created by microdispensing the ink. Then, the ink is dried at 125 °C for one hour. Next, the 3D-printed substrate is placed upside down to dispense the top metal layer after careful alignment using a process camera on the nScrypt

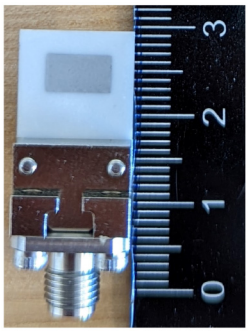

(a) Top Commercial YSZ + Pt

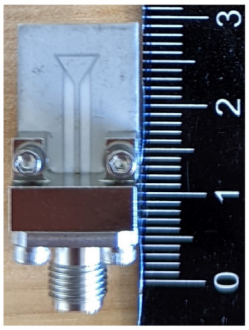

(b) Bottom Commerical YSZ + Pt

FIGURE 10. AM antenna using commercial YSZ and Ferro ESL 5520 platinum ink (scale in cm).

TABLE 3. Dimensions of the designed antenna based on 3D-printed YSZ (units in mm).

w_p	l_p	l_c	l_s	w_s
8.8	4.37	10	48.67	15.17
w_l	g	l_f	l_{stub}	w_{stub}
0.6	0.7	8.02	3.23	4.33
g_{stub}				
0.36				

(a) Top layer

(b) Bottom layer

FIGURE 11. Micro-dispensed platinum ink on the 3D-printed YSZ substrate before drying process.

system to reduce layer misregistration. Finally, the platinum ink is dried once the top patch is patterned by microdispensing.

Once the platinum layers of each side of the antenna are dried, the platinum ink is sintered with a ramp-up rate of 30°C/min until reaching 980 °C, where the temperature is held by 10 min, and then the furnace cools down

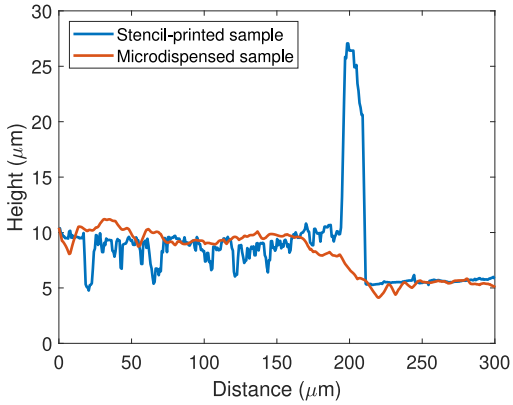

FIGURE 12. Surface profile of stencil-printed and micro-dispensed platinum ink after sintering process.

until ambient. Fig. 11 and 13 show the surface of micro-dispensed ink on the 3D-printed YSZ substrate before the drying process and after the sintering process, respectively. The mean thickness of the metal layer is 5 μm, which is similar to the stencil-printed metal layer. Note that both, CB028 and the Pt ink are optimized by the manufacturer for screen printing, and not for stencil printing. The interaction between the microdispensed ink and the substrate surface creates a tapered geometry on the edges of the conductor [35]. Additionally, since the ink spreads after dispensing, the thickness increases gradually from the edges, while the stencil-printed metal layer has steeper surface edges. Fig. 12 shows the measured surface profile of the transition area of the sintered trace made by the stencil printing process and the microdispensing process. The ink spread observed in the microdispensing process is a consequence of the rheological properties of the ink, leading to a gradual thickness increment from the edges. The sharp edges observed in the stencil printing result from leaving the PET stencil during the ink cure since it promotes the accumulation of Ag particles on the stencil wall. A favorable wettability contact angle at the stencil wall is presumed responsible for the surface profile's peak, creating a concave meniscus. Therefore, as the binder evaporates, the conductive particles accumulate on the edges to replace the loss of the organic material, leading to a gradual thickness increment creating sharp edges. Besides, since stencil printing is performed manually, there is limited control during the process, which can lead to a surface with more pores than the microdispensed one. Note that the stencil printing samples serve benchmarking purposes, but their quality is not as per industry standards. In addition, the sharp edges can be smothered after carefully scrapping the cured surface or removing it by laser.

Fig. 13 exhibits the top view and bottom view of the fully AM coupled-fed antenna made of the 3D-printed YSZ substrate and the micro-dispensed platinum ink after being sintered. The surface scratches of the bottom layer are due to manipulation of the antenna, but they do not have any impact on the antenna performance.

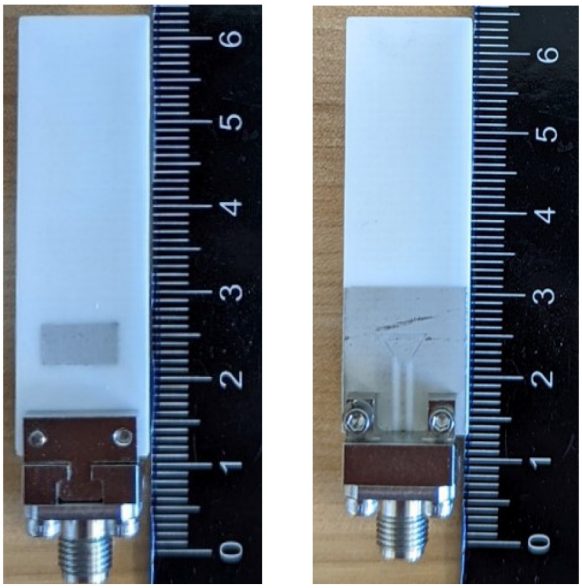

(a) Top AM YSZ + Pt (b) Bottom AM YSZ + Pt

FIGURE 13. Fully AM antenna using 3D-printed YSZ and Ferro ESL 5520 platinum ink (scale in cm).

V. ANTENNA EXPERIMENTAL RESULTS

A. ANTENNA CHARACTERIZATION

The couple-fed antenna based on platinum ink and the commercial YSZ is the reference antenna during the characterization process to assess the antenna performance of the fully AM coupled-fed made of platinum ink and the 3D-printed YSZ. The resonant response of both antennas is measured using a Keysight E5071C ENA calibrated from 2 GHz to 8 GHz by a Keysight N4433A ECal module. Fig. 14 exhibits the S11 of each antenna over the frequency, where the measured results agree with the simulated outcome in each case. The reference antenna resonates at 5.09 GHz, while the fully AM antenna has a resonant frequency at 3.5 GHz and 4.1 GHz. Since the 3D-printed YSZ substrate shows similar electromagnetic properties to the commercial YSZ substrate, the fully AM antenna is designed to resonate at a lower frequency because the 3D-printed substrate is thicker than the commercial one, avoiding high-order propagation in the couple feeding.

The radiation pattern of the manufactured antennas is measured from 2 GHz to 6 GHz by an ETS-Lindgren anechoic chamber. The frequency step is set at 10 MHz, while the angular step is 5 deg for the azimuth axis and elevation axis. Fig. 15 show the simulated 3D radiation pattern at 5.09 GHz and the location of the E-plane and H-plane of the designed antenna using the commercial YSZ and stencil-printed platinum ink.

Fig. 16 displays a good agreement between the measured and simulated radiation pattern of the reference antenna for the E-plane and H-plane at 5.09 GHz. Also, the reference antenna exhibits a measured gain of 1.29 dBi at $\theta = 60°$, and a front-back ratio of 6.16 dB.

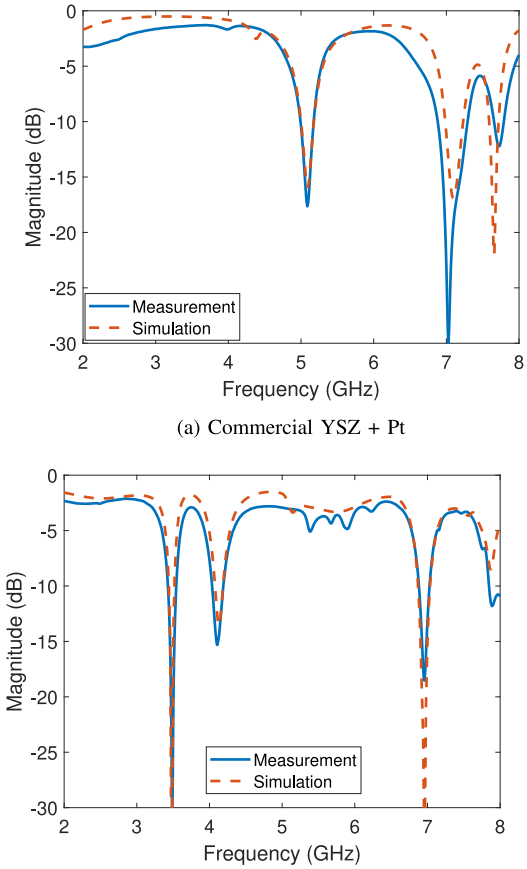

(a) Commercial YSZ + Pt

(b) 3D-printed YSZ + Pt

FIGURE 14. Measured and simulated S11 for the manufactured antennas using platinum ink.

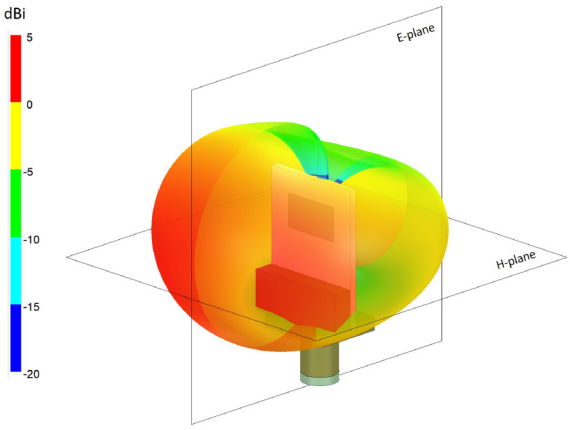

FIGURE 15. Simulated 3D radiation pattern of the designed antenna at 5.09 GHz with E-plane and H-plane location.

The antenna gain is plotted as a function of the frequency from 2 GHz to 6 GHz to verify the radiation characteristics of the fully AM antenna at both resonant frequencies, i.e., at 3.5 GHz and 4.11 GHz. Fig. 17 shows that the measured and simulated antenna gain has two peaks around the resonant frequencies. However, the resonant response at 3.5 GHz does not radiate as efficiently as at 4.11 GHz.

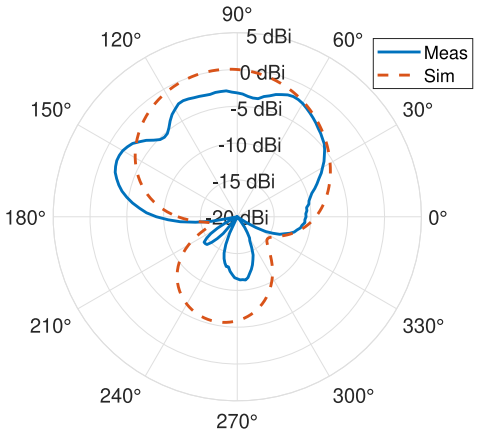

(a) E-plane

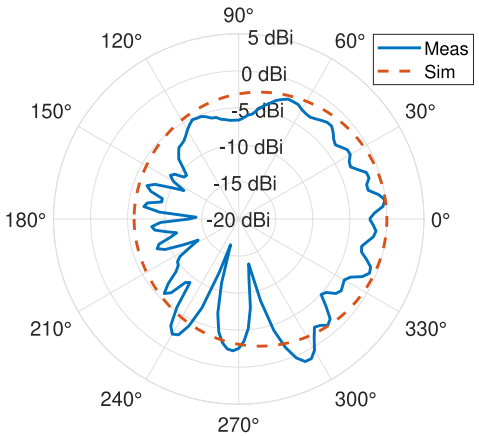

(b) H-plane

FIGURE 16. Measured and simulated radiation pattern at 5.09 GHz of the manufactured antenna using commercial YSZ and platinum ink.

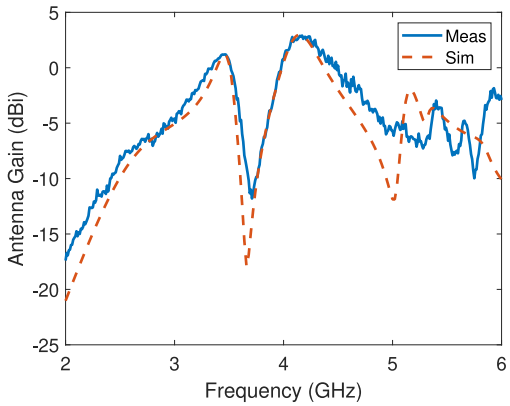

FIGURE 17. Measured and simulated antenna gain of the fully AM antenna (in dBi) from 2 GHz to 6 GHz.

The antenna radiation efficiency is simulated and measured, as shown in Fig. 18. The simulated radiation efficiency is extracted from the antenna parameter report of Ansys HFSS, while the measured radiation efficiency is extracted summary report of the anechoic chamber. The measured radiation efficiency trace shows that the radiation efficiency is 60% and 85% at 3.5 GHz and 4.11 GHz,

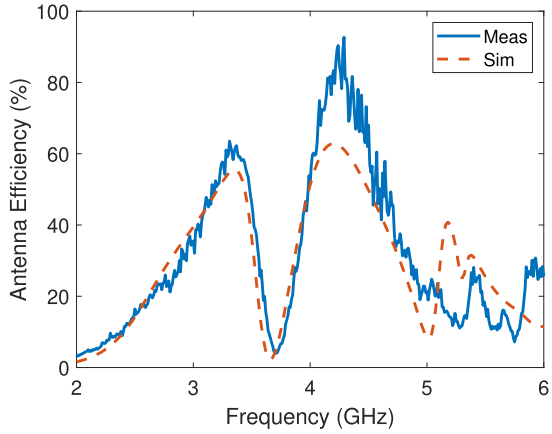

FIGURE 18. Measured and simulated radiation efficiency of the fully AM antenna from 2 GHz to 6 GHz.

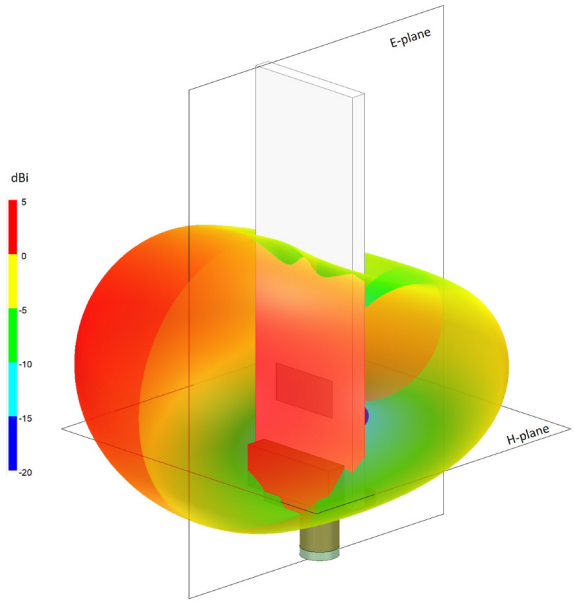

FIGURE 19. Simulated 3D radiation pattern of the fully AM antenna at 4.11 GHz with E-plane and H-plane location.

respectively, which confirms that the antenna does not radiate efficiently at 3.5 GHz.

Fig. 19 exhibit the simulated 3D radiation pattern at 4.11 GHz and the location of the E-plane and H-plane of the fully AM antenna using 3D-printed YSZ and micro-dispensed platinum ink.

The simulated and measured E-plane and H-plane at 4.11 GHz of the fully AM antenna are shown in Fig. 20. The measured antenna gain is 2.59 dBi at $\theta = 60°$, and the measured front-back ratio is 9.62 dB.

B. RF CHARACTERIZATION AFTER THERMAL FATIGUE

This paper shows RF specimens made of ceramic substrates and coated layers of conductive ink, which have different coefficient thermal expansion (CTE). If there is an evident CTE mismatch, the exposure of these samples to thermal

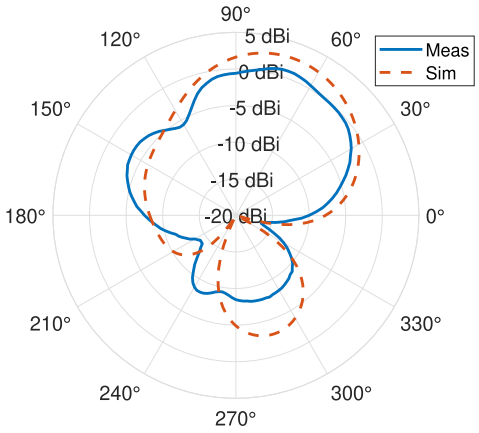

(a) E-plane

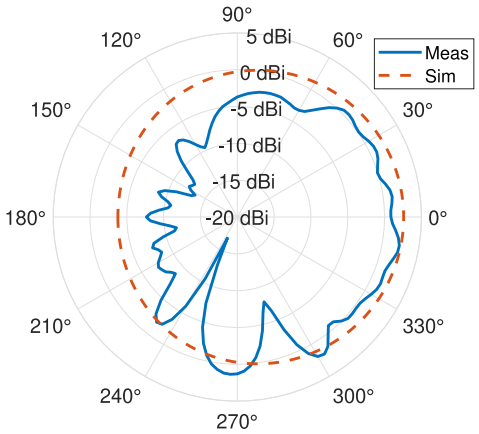

(b) H-plane

FIGURE 20. Simulated and measured radiation pattern at 4.11 GHz of the manufactured antenna using 3D-printed YSZ and platinum ink.

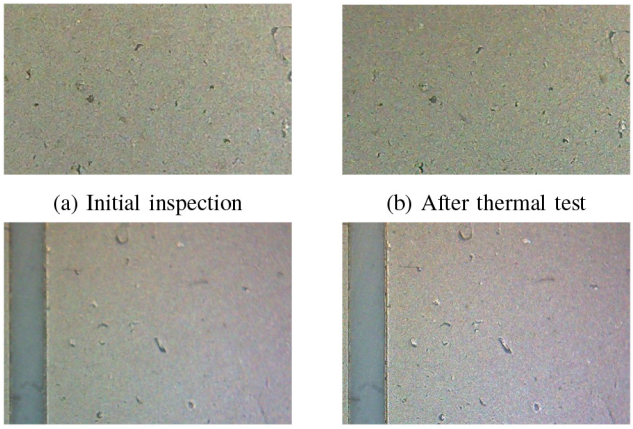

(a) Initial inspection (b) After thermal test

(c) Initial inspection (d) After thermal test

FIGURE 21. Visual inspection of a platinum CPW on a commercial YSZ substrate before and after the thermal test.

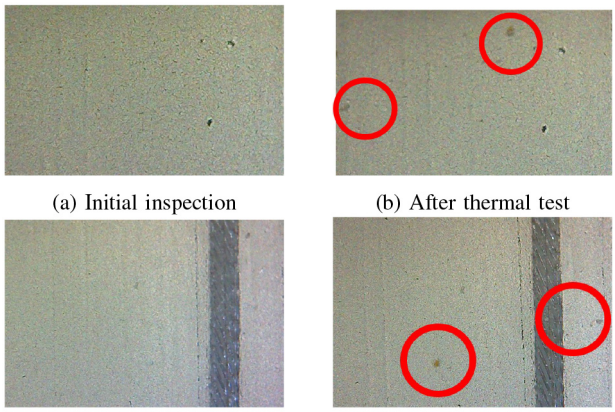

(a) Initial inspection (b) After thermal test

(c) Initial inspection (d) After thermal test

FIGURE 22. Visual inspection of a platinum CPW on a 3D-printed YSZ substrate before and after the thermal test.

cycles will lead to micro-damage caused by the thermal strain and internal stress that control the deformation of each material, where the thermal fatigue can produce microscopic cracks, pinholes, and peeling off of the conductive layer.

Platinum stencil-printed specimens on two commercial YSZ substrates and a 3D-printed YSZ substrate are exposed to a fluctuating high-temperature environment, where the samples are heated from ambient to 600 °C at a rate of 27 °C/min, and they are soaked at the peak temperature for 30 min. Then, the samples cool down to 32 °C, and a new cycle begins. The thermal cycle is repeated nine times, but the specimens are inspected by the microscope every three cycles to identify any evidence of thermal fatigue.

Fig. 21 shows the initial inspection before the thermal test and the final inspection after the ninth cycle of the platinum CPW over the commercial YSZ substrate at two different locations. However, these results can be extended with similar behavior to the rest of the sample. Based on the visual inspection of the conductive ink before and after the thermal cycling, no thermal fatigue is evidenced after the nine high-temperature cycles. This result suggests that the CTE mismatch between the conductive and dielectric layers is not large enough to generate damage to the sample during thermal cycling, which means there is no evident mismatch of CTE between the commercial YSZ substrate and the sintered platinum layer.

Fig. 22 shows the initial and final visual inspection of the platinum CPW on a 3D-printed YSZ substrate after nine high-temperature cycles. In this case, it is noted that the sintered platinum layer exhibits dark spots in different sections of the samples after the third cycle. However, their size, shape, and color remain the same after finishing the thermal test. Besides the dark spots, there is no sign of any visible micro-damage in the sample.

The S-parameters of the platinum CPW samples are measured again from 2 GHz to 6 GHz to identify if there is any non-visible micro-damage of the high-temperature samples. A silver CPW sample with no thermal cycle is used as a control sample and is measured simultaneously on all the S-parameter measurements to detect deviations in the vector network analyzer calibration. Fig. 23a exhibits the magnitude of S_{21} of the silver CPW sample and the platinum CPW samples before the thermal test and after the nine high-temperature cycles. The reference CPW and the

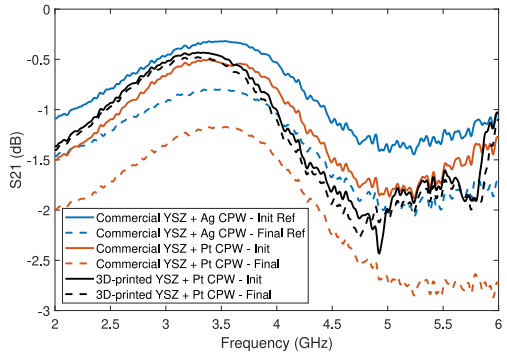

(a) S21 - magnitude

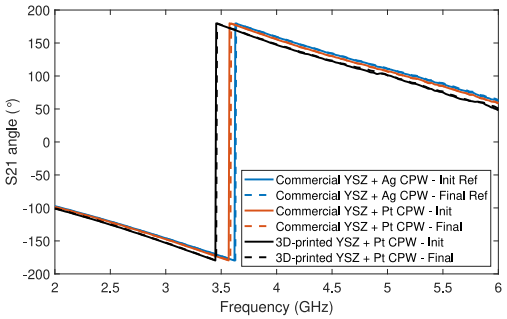

(b) S21 - angle

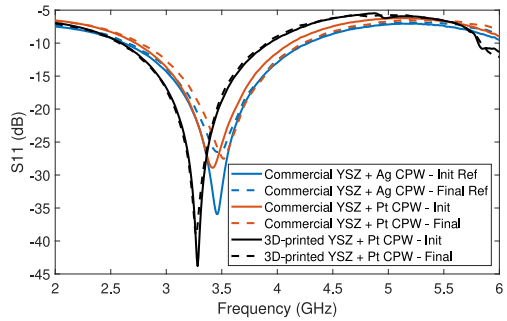

(c) S11 - magnitude

FIGURE 23. Measured S-parameters of CPW samples before and after the thermal test.

platinum CPW on the commercial YSZ show ∼0.5 dB degradation of the S_{21} at 2 GHz, getting slightly worst as the frequency increases. However, the platinum CPW over the 3D-printed substrate shows minimal variation after the thermal test. Fig. 23b and Fig. 23c exhibit minimal variations in the angle of S_{21} and the magnitude of S_{11} relative to the thermal test.

Fig. 24 exhibits the dissipative losses of the CPW, which are calculated by the well-know equation:

$$DL_{dB} = 10\log\Big(|S_{21}|^2/\Big(1-|S_{11}|^2\Big)\Big) \tag{3}$$

The dissipative losses show similar degradation as shown in Fig. 23a. However, the reference sample was not exposed intentionally to any thermal test to have a golden sample on the experiment control of the thermal cycling. Therefore, the variation of S_{21} and the dissipative losses after cycling can be related to the variation of the position and pressure of the probe during the calibration and probing test.

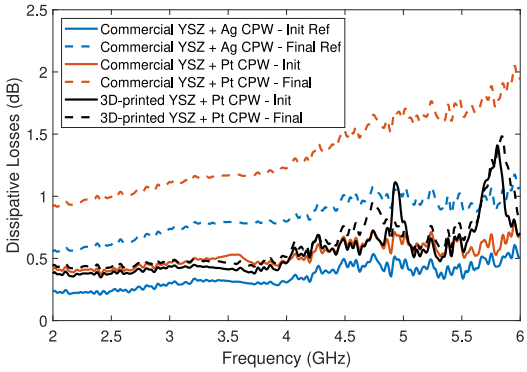

FIGURE 24. Calculated dissipative losses of the CPW samples before and after the thermal test.

Furthermore, since the platinum CPW over the 3D-printed substrate shows minimal variation after the thermal test, the results suggest that the thermal stress applied to samples is not enough to create thermal fatigue. Therefore, the nine high-temperature cycles applied to the specimens do not lead to any appreciable degradation of the RF performance of the CPWs.

VI. CONCLUSION

This work shows a successful additive manufacturing process to make a high-temperature antenna by metalizing the top and bottom sides of a 3D-printed YSZ substrate using microdispensing conductive ink that endures high temperatures. As a result, the 3D-printed antenna exhibits a gain of 2.5 dBi, which is better than a half-wave dipole antenna. Besides, the antenna has a bandwidth of 160 MHz for return loss $\geq$ 10 dB at 4.1 GHz, which is better than a traditional microstrip patch antenna that is typically less than 3%. Furthermore, the coplanar waveguide lines made of 3D-printed YSZ and platinum ink do not show thermal fatigue or degradation of the RF performance of the passive component after exposing them to nine short-time high-temperature cycles that reach up to 600 °C. Future research includes extending the high-temperature endurance studies to evaluate the antenna survivability for long-duration missions.

ACKNOWLEDGMENT

The authors would like to thank Embry-Riddle Aeronautical University for the financial support of this work and acknowledge the Friedman Chair at Youngstown State University.

REFERENCES

[1] Y. Liu, S. Zhang, and Y. Gao, "A high-temperature stable antenna array for the satellite navigation system," *IEEE Antennas Wireless Propag. Lett.*, vol. 16, pp. 1397–1400, 2017.

[2] C. Wang et al., "Coupling model and electronic compensation of antenna-radome system for hypersonic vehicle with effect of high-temperature ablation," *IEEE Trans. Antennas Propag.*, vol. 68, no. 3, pp. 2340–2355, Mar. 2020.

[3] H. Weng, F. L. Duan, Z. Xie, S. Liu, Z. Ji, and Y. Zhang, "LiNbO3-based SAW sensors capable to measure up to 1100°C high temperature," *IEEE Sensors J.*, vol. 20, no. 21, pp. 12679–12683, Nov. 2020.

[4] W. C. Wilson and G. M. Atkinson, "Passive wireless sensor applications for NASA's extreme aeronautical environments," *IEEE Sensors J.*, vol. 14, no. 11, pp. 3745–3753, Nov. 2014.
[5] N. P. Padture, "Advanced structural ceramics in aerospace propulsion," *Nat. Mater.*, vol. 15, no. 8, pp. 804–809, 2016.
[6] T. Kremic and G. W. Hunter, "Long-lived in-situ solar system explorer (LLISSE): Potential contributions to the next decade of solar system exploration," in *Proc. VEXAG Annu. Meeting*, 2019, pp. 1–7.
[7] K. V. Kaaden et al., "Mercury exploration: Looking to the future," in *Proc. Lunar Planet. Sci. Conf.*, 2019, pp. 1–2.
[8] D. Zhu, "Aerospace ceramic materials: Thermal, environmental barrier coatings and SiC/SiC ceramic matrix composites for turbine engine applications," Nat. Aeronaut. Space Admin., Washington, DC, USA, Rep. NASA/TM-2018-219884, 2018.
[9] W. G. Fahrenholtz, "A historical perspective on research related to ultra-high temperature ceramics," in *Ultra-High Temperature Ceramics: Materials for Extreme Environment Applications*. Hoboken, NJ, USA: Wiley, 2014, ch. 2, pp. 6–32.
[10] J. Li, C. Guo, L. Mao, J. Xiang, G. Huang, and T. Yuan, "Monolithically 3-D printed hemispherical resonator waveguide filters with improved out-of-band rejections," *IEEE Access*, vol. 6, pp. 57030–57048, 2018.
[11] J. Castro, E. A. Rojas-Nastrucci, A. Ross, T. M. Weller, and J. Wang, "Fabrication, modeling, and application of ceramic-thermoplastic composites for fused deposition modeling of microwave components," *IEEE Trans. Microw. Theory Techn.*, vol. 65, no. 6, pp. 2073–2084, Jun. 2017.
[12] Y. Oh et al., "Microwave dielectric properties of zirconia fabricated using NanoParticle jetting," *Additive Manuf.*, vol. 27, pp. 586–594, May 2019. [Online]. Available: http://www.sciencedirect.com/science/article/pii/S2214860419301265
[13] S. Wang et al., "Radar cross-section reduction of helical antenna by replacing metal with 3-D printed Zirconia ceramic," *IEEE Antennas Wireless Propag. Lett.*, vol. 19, no. 2, pp. 350–354, Feb. 2020.
[14] S. L. Yu et al., "Advanced manufacturing of passive wireless high-temperature pressure sensor using 3-D laser machining," in *Proc. IEEE 22nd Annu. Wireless Microw. Technol. Conf. (WAMICON)*, 2022, pp. 1–4.
[15] H. Al Mehedi et al., "Increased chemical reactivity of single-walled carbon nanotubes on oxide substrates: *In situ* imaging and effect of electron and laser irradiations," *Nano Res.*, vol. 9, no. 2, pp. 517–529, Feb. 2016.
[16] A. Desireddy et al., "Ultrastable silver nanoparticles," *Nature*, vol. 501, no. 7467, pp. 399–402, Sep. Jan.Sep. 2013.
[17] S. Sohn et al., "Noble metal high entropy alloys," *Scripta Materialia*, vol. 126, pp. 29–32, Jan. 2017.
[18] L.-Y. Chen, P. G. Neudeck, D. J. Spry, G. M. Beheim, and G. W. Hunter, "Electrical performance of a 32-I/O HTCC alumina package for high-temperature microelectronics," *J. Microelectron. Electron. Packag.*, vol. 14, no. 1, pp. 11–16, 2017.
[19] X. Ren, S. Ebadi, Y. Chen, L. An, and X. Gong, "Characterization of SiCN ceramic material dielectric properties at high temperatures for harsh environment sensing applications," *IEEE Trans. Microw. Theory Techn.*, vol. 61, no. 2, pp. 960–971, Feb. 2013.
[20] H. Cheng, X. Ren, S. Ebadi, Y. Chen, L. An, and X. Gong, "Wireless passive temperature sensors using integrated cylindrical resonator/antenna for harsh-environment applications," *IEEE Sensors J.*, vol. 15, no. 3, pp. 1453–1462, Mar. 2015.
[21] H. Cheng, S. Ebadi, and X. Gong, "A low-profile wireless passive temperature sensor using resonator/antenna integration up to 1000 °C," *IEEE Antennas Wireless Propag. Lett.*, vol. 11, pp. 369–372, 2012.
[22] Y. Ji, Q. Tan, H. Wang, W. Lv, H. Dong, and J. Xiong, "A novel surface *LC* wireless passive temperature sensor applied in ultra-high temperature measurement," *IEEE Sensors J.*, vol. 19, no. 1, pp. 105–112, Jan. 2019.
[23] T. Karacolak, R. V. K. G. Thirumalai, J. N. Merrett, Y. Koshka, and E. Topsakal, "Silicon carbide (SiC) antennas for high-temperature and high-power applications," *IEEE Antennas Wireless Propag. Lett.*, vol. 12, pp. 409–412, 2013.
[24] J. A. Thiele and M. P. da Cunha, "Platinum and palladium high-temperature transducers on langasite," *IEEE Trans. Ultrason., Ferroelectr., Freq. Control*, vol. 52, no. 4, pp. 545–549, Apr. 2005.
[25] P. M. Davulis and M. P. da Cunha, "A full set of langatate high-temperature acoustic wave constants: Elastic, piezoelectric, dielectric constants up to 900°C," *IEEE Trans. Ultrason., Ferroelectr., Freq. Control*, vol. 60, no. 4, pp. 824–833, Apr. 2013.
[26] J. E. Rogers, Y. Yoon, M. Sheplak, and J. W. Judy, "A passive wireless microelectromechanical pressure sensor for harsh environments," *J. Microelectromech. Syst.*, vol. 27, no. 1, pp. 73–85, 2018.
[27] M. Pereira da Cunha, T. Moonlight, R. Lad, G. Bernhardt, and D. J. Frankel, "P4L-1 enabling very high temperature acoustic wave devices for sensor frequency control applications," in *Proc. IEEE Ultrasonics Symp. Process.*, 2007, pp. 2107–2110.
[28] M. P. da Cunha et al., "Wireless acoustic wave sensors and systems for harsh environment applications," in *Proc. IEEE Topical Conf. Wireless Sens. Sens. Netw.*, 2011, pp. 41–44.
[29] *Standard Terminology for Additive Manufacturing Technologies*[1,2], ASTM Standard F2792-12A, 2012.
[30] B. de Gans, P. Duineveld, and U. Schubert, "Inkjet printing of polymers: State of the art and future developments," *Adv. Mater.*, vol. 16, no. 3, pp. 203–213, 2004.
[31] B. Derby and N. Reis, "Inkjet printing of highly loaded particulate suspensions," *MRS Bull.*, vol. 28, no. 11, pp. 815–818, 2003.
[32] B. Mummareddy et al., "Mechanical properties of material jetted zirconia complex geometries with hot isostatic pressing," *Adv. Ind. Manuf. Eng.*, vol. 3, Nov. 2021, Art. no. 100052.
[33] S. L. Yu and E. A. Rojas-Nastrucci, "Characterization of microdispensed dielectric materials for direct digital manufacturing using coplanar waveguides," in *Proc. IEEE 20th Wireless Microw. Technol. Conf. (WAMICON)*, 2019, pp. 1–3.
[34] C. R. Mejias-Morillo and E. A. Rojas-Nastrucci, "Z-meandering miniaturized patch antenna using additive manufacturing," in *Proc. IEEE Radio Wireless Symp. (RWS)*, 2020, pp. 31–34.
[35] E. A. Rojas-Nastrucci et al., "Characterization and modeling of K-band coplanar waveguides digitally manufactured using pulsed picosecond laser machining of thick-film conductive paste," *IEEE Trans. Microw. Theory Techn.*, vol. 65, no. 9, pp. 3180–3187, Sep. 2017.
[36] T. P. Ketterl et al., "A 2.45 GHz phased array antenna unit cell fabricated using 3-D multi-layer direct digital manufacturing," *IEEE Trans. Microw. Theory Tech.*, vol. 63, no. 12, pp. 4382–4394, Dec. 2015.
[37] D. A. Roberson, R. B. Wicker, L. E. Murr, K. Church, and E. MacDonald, "Microstructural and process characterization of conductive traces printed from Ag particulate inks," *Materials*, vol. 4, no. 6, pp. 963–979, 2011. [Online]. Available: https://www.mdpi.com/1996-1944/4/6/963
[38] H. El-halabi, H. Issa, E. Pistono, D. Kaddour, S. Abou-Chahine, and P. Ferrari, "Compact low-pass stepped impedance filters with enhanced out of band response," *Microw. Opt. Technol. Lett.*, vol. 59, no. 8, pp. 1791–1800, 2017.
[39] W. Heinrich, F. Schnieder, and T. Tischler, "Dispersion and radiation characteristics of conductor-backed CPW with finite ground width," in *IEEE MTT-S Int. Microw. Symp. Dig.*, vol. 3, 2000, pp. 1663–1666.
[40] E. A. Rojas-Nastrucci, J. Nussbaum, T. M. Weller, and N. B. Crane, "Meshed rectangular waveguide for high power, low loss and reduced weight applications," in *IEEE MTT-S Int. Microw. Symp. Dig.*, 2016, pp. 1–4.

CARLOS R. MEJIAS-MORILLO received the B.S. and M.S. degrees in electrical engineering from the Universidad de Carabobo, Valencia, Venezuela, in 2008 and 2014, respectively. He is currently pursuing the Ph.D. degree in the electrical engineer and computer science program with Embry–Riddle Aeronautical University, Daytona Beach, FL, USA, where he is currently a Member of Wireless Devices and Electromagnetics Laboratory. His research interests are additive manufacturing applied to passive RF and microwave devices, novel 3-D antennas, flexible packaging for wearables, and wireless passive sensor networks. He is actively researching about 3-D antennas and antenna-in-package for harsh environments, especially for aerospace applications. Also, he holds one U.S. patent related to 3-D antennas. In 2019, he received the Best Paper Award for the paper titled "UHF RFID-Based Additively Manufactured Passive Wireless Sensor for Detecting Micrometeoroid and Orbital Debris Impacts," which was issued by the 2019 IEEE International Conference on Wireless for Space and Extreme Environments.

JAYAPRAKASH B. SHIVAKUMAR is currently pursuing the degree in senior aerospace engineering with Embry–Riddle Aeronautical University, where he currently works as a Research Assistant with Wireless Devices and Electromagnetics Laboratory, focusing on antenna and RF design and fabrication. Additionally, he has experience developing hybrid-electric power plant systems and batteries for aircraft and developing their digital twin.

SENG LOONG YU received the B.S. degree in electrical engineering from the University of South Florida in 2015, and the M.S. degree in electrical engineering from San Jose State University in 2017. He is currently pursuing the Ph.D. degree in electrical engineering and computer science with Embry–Riddle Aeronautical University, Daytona Beach, FL, USA where he conducts his research in the Wireless Devices and Electromagnetics Laboratory. During his time at the University of South Florida, he was an undergraduate research assistant in the Center for Wireless and Microwave Information Systems Laboratory. While at San Jose State University, he studied CMOS RF and analog IC design and was a Lab Instructor for the undergraduate electronics course. His current research interests are in advanced manufacturing and dielectric characterization methods for high-temperature mm-wave antennas. He is exploring laser-assisted additive manufactured LTCC materials to be used in high-temperature environments. Additionally, he was with Qorvo Inc. working as a BAW Research and Development Engineering intern working on developing filter modules with advanced packaging.

BLAKE ROBERTS , photograph and biography not available at the time of publication.

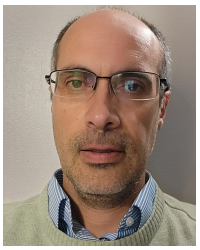

PEDRO CORTES is currently an Associate Professor with the Department of Civil/Environmental and Chemical Engineering Program as well as with the Materials Science and Engineering Program, Youngstown State University. His research interests include the area of 3-D printing, including smart and multifunctional materials, composite structures, and metal-ceramic systems. His research work has been funded through the U.S. Department of Transportation, the Department of Defense, NASA, the National Science Foundation, and the Ohio Federal Research Network. He has served twice as a Faculty Fellow of the Wright-Patterson Air Force Base.

ERIC MACDONALD (Senior Member, IEEE) received the Doctoral degree in electrical and computer engineering from the University of Texas at Austin in 2002. He is a Professor of Aerospace and Mechanical Engineering and Murchison Chair with the University of Texas at El Paso and serves as the Associate Dean of Research and Graduate Studies for the College of Engineering. He worked in industry for 12 years with IBM and Motorola and subsequently co-founded a startup specializing in CAD software and the startup was acquired by a firm in Silicon Valley. He held faculty fellowships with NASA's Jet Propulsion Laboratory and U.S. Navy Research and was awarded a U.S. State Department Fulbright Fellowship in South America. His research interests include 3-D printed multifunctional applications and process monitoring in additive manufacturing with instrumentation and computer vision for improved quality and yield. As a Co-Founding Editor of the *Additive Manufacturing* (Elsevier), he has helped direct the academic journal to have highest impact factor among all manufacturing journals worldwide. He has recently been involved in the commissioning of a second partner journal, *Additive Manufacturing Letters*, upon which he serves as the Editor-in-Chief. His recent projects include 3-D printing of structures such as nanosatellites with structurally embedded electronics — one of which was launched into Low Earth Orbit in 2013 and a replica of which was on display at the London Museum of Science. He has over 100 peer-reviewed publications, dozens of patents, one of which was licensed by Sony and Toshiba from IBM. He is a member of ASME and ASEE, and a registered Professional Engineer in the USA state of Texas.

ANTON V. POLOTAI received the Doctoral degree from Materials Science Institute, National Academy of Science of Ukraine in 2002. He is a Senior Scientist with Vibrantz Technologies. He worked as a Research Associate with the Center for Dielectric Studies of the Pennsylvania State University, State College, PA, USA, performing research on advance processing for ceramic materials. In 2008, he joined industry (MRA Laboratories, Inc., Ferro Corporation, and Vibrantz Technologies) continuing research and development in the field of formulated ceramic materials for electronic application. He is an author and the coauthor of more than 30 scientific papers and numerous conference publications.

EDUARDO A. ROJAS-NASTRUCCI received the M.S. and Ph.D. degrees in electrical engineering from the University of South Florida in 2014 and 2017, respectively. He joined the Embry–Riddle Aeronautical University (ERAU) in 2017, where he is an Associate Professor. His research interests are in microwave/mm-wave circuits and antenna applications of additive manufacturing and wireless sensing for harsh environments; in the context of aviation and space systems. He is the co-director of Wireless Devices and Electromagnetics Laboratory with ERAU. He has more than 40 peer-reviewed publications and six U.S. patents. He received the CAREER Award from the National Science Foundation in 2019; the 2022 Jet Propulsion Laboratory Faculty Fellowship; the 2020 Most Promising Engineer Award, Ph.D. Education category, from the Great Minds in Stem organization; and the ERAU's 2021 Abas Sivjee Outstanding Research Award. He is a member of the IEEE MTT-S Technical Committees 4, 26, and 29; and the RTCA SC-236 Committee for Standards for Wireless Avionics Intra-Communication System within 4200–4400 MHz.